

Exploring Mechanisms of Variability and Predictability of Atlantic Meridional Overturning Circulation in Two Coupled Climate Models

ROSS TULLOCH AND JOHN MARSHALL

Department of Earth, Atmospheric and Planetary Sciences, Massachusetts Institute of Technology, Cambridge, Massachusetts

(Manuscript received 19 August 2011, in final form 22 November 2011)

ABSTRACT

Multidecadal variability in the Atlantic meridional overturning circulation (AMOC) of the ocean is diagnosed in the NCAR Community Climate System Model, version 3 (CCSM3), and the GFDL Coupled Model (CM2.1). Common diagnostic approaches are applied to draw out similarities and differences between the two models. An index of AMOC variability is defined, and the manner in which key variables covary with it is determined. In both models the following is found. (i) AMOC variability is associated with upper-ocean (top 1 km) density anomalies (dominated by temperature) on the western margin of the basin in the region of the Mann eddy with a period of about 20 years. These anomalies modulate the trajectory and strength of the North Atlantic Current. The importance of the western margin is a direct consequence of the thermal wind relation and is independent of the mechanisms that create those density anomalies. (ii) Density anomalies in this key region are part of a larger-scale pattern that propagates around the subpolar gyre and acts as a “pacemaker” of AMOC variability. (iii) The observed variability is consistent with the primary driving mechanism being stochastic wind curl forcing, with Labrador Sea convection playing a secondary role. Also, “toy models” of delayed oscillator form are fitted to power spectra of key variables and are used to infer “quality factors” (Q-factors), which characterize the bandwidth relative to the center frequency and hence AMOC predictability horizons. The two models studied here have Q-factors of around 2, suggesting that prediction is possible out to about two cycles, which is likely larger than the real AMOC.

1. Introduction

The Atlantic meridional overturning circulation (AMOC) of the ocean plays a central role in climate, transporting heat across the equator into the North Atlantic Ocean basin. It is thought to modulate, for example, sea surface temperature (SST) and mediate sea ice extent in high northern latitudes (Kushnir 1994; Mahajan et al. 2011a). The AMOC in coupled climate models often exhibits pronounced decadal variability that might be reflected in, and inherited by, other parts of the climate system. Moreover, if decadal AMOC variability is associated with slow ocean processes that are predictable, then such predictability (if it exists) might be leveraged and exploited in coupled climate models used for climate change prediction and

attribution—see Marshall et al. (2001a) and Hurrell et al. (2006) for a background discussion.

Currently there is intense interest in understanding the AMOC, documenting how it varies in observations (Kushnir 1994; Delworth and Mann 2000; Johns et al. 2011) and in models (Weaver et al. 1993; Delworth et al. 1993; Griffies and Tziperman 1995; Jayne and Marotzke 2001; Dai et al. 2005; Dong and Sutton 2005; Jungclauss et al. 2005; Danabasoglu 2008; Tziperman et al. 2008; Hawkins and Sutton 2009) and identifying the causes of that variability. Thus far it has not been possible to unambiguously identify a single driving mechanism and indeed there seems to be much model dependence in AMOC variability—see Marshall et al. (2001b), Danabasoglu (2008), Yoshimori et al. (2010), Kwon and Frankignoul (2012), and Sévellec and Fedorov (2011, and references therein).

AMOC variability diagnosed in models typically falls into one of the following types:

- 1) self-sustained internal (ocean only) oscillations (Colin de Verdière and Huck 1999; Te Raa et al. 2004; Zhu and Jungclauss 2008; Buckley et al. 2012),

Corresponding author address: Ross Tulloch, Department of Earth, Atmospheric and Planetary Sciences, Massachusetts Institute of Technology, 77 Massachusetts Ave., Cambridge, MA 02139.
E-mail: tulloch@mit.edu

- 2) a damped oceanic mode stochastically excited by the atmosphere (Delworth et al. 1993; Griffies and Tziperman 1995; Delworth and Greatbatch 2000; Dai et al. 2005; Dong and Sutton 2005; Sévellec and Fedorov 2011; Frankcombe and Dijkstra 2009) and/or freshwater interactions with the Arctic (Jungclauss et al. 2005; Delworth et al. 1997; Olsen et al. 2008), and
- 3) coupled atmosphere–ocean modes (Weaver and Valcke 1998; Eden and Willebrand 2001; Oka and Hasumi 2006).

Some of the present uncertainty reflects the undoubted complexity of the processes at work. However, this is compounded by the fact that different diagnostic methods are employed by different investigators who come to the problem with differing viewpoints. Here we attempt to rationalize the situation somewhat. In section 2 we diagnose AMOC variability in two different coupled climate models—the National Center for Atmospheric Research (NCAR) Community Climate System Model, version 3 (CCSM3), and the Geophysical Fluid Dynamics Laboratory Climate Model, version 2.0 (GFDL CM2.1). An index of AMOC variability is defined and the manner in which key variables covary with it is used to draw out aspects of underlying mechanisms and similarities and differences between the two models. We draw attention to the role of subsurface density anomalies that abut the continental shelf on the western margin of the Atlantic basin in the region of the Mann eddy. This region is located at the latitude at which the mean AMOC is a maximum and where it exhibits maximum variability in the two models. In section 3 we fit “toy models” of delayed oscillator form to observed spectra of key variables and use them to infer “Q-factors,” characterizing the bandwidth relative to the center frequency, and hence AMOC predictability horizons. Finally, in section 4, we conclude, drawing out aspects that might pertain to the real, rather than the modeled, ocean.

2. Variability in the Atlantic Ocean in two coupled climate models

Here we explore the variability of AMOC in 500-yr control integrations of the NCAR CCSM3 and the GFDL CM2.1. The detailed configurations of each model are described in the appendix. AMOC variability has been studied before in these two models, as we now briefly describe.

In Danabasoglu (2008), deep convection in the Labrador Sea region was identified as a key precursor to decadal AMOC variability in CCSM3, and complicated interactions between the MOC and deep-water formation, the North Atlantic Oscillation (NAO), and the subpolar gyre

circulation are identified as drivers of MOC variability. Yoshimori et al. (2010) analyzed a low-resolution version of CCSM3 and argued that variability involves an interaction between advection of salt and surface density in the subpolar gyre, with a connection to the NAO. A positive feedback involving eddy activity in the atmosphere was invoked. Meanwhile, Kwon and Frankignoul (2012) identified regimes of high and low AMOC variability in CCSM3. The first regime (studied by Danabasoglu 2008) has a very regular 20-yr oscillation and the second regime has red noise–like variability. They concluded that the variability in the second regime could be understood as a damped oceanic mode that is stochastically excited by the NAO. They also noted that a delayed positive feedback caused by changes in horizontal ocean circulation increased AMOC persistence from 5 to 10 years.

Zhang (2008) noted that AMOC variability in CM2.1 is associated with a dipole in subsurface temperature anomalies. A positive AMOC is associated with negative temperature anomalies in the Gulf Stream region and slightly weaker positive temperature anomalies in the subpolar gyre, indicating that a strengthening of the AMOC in CM2.1 is associated with a weakening of the subpolar gyre. Zhang et al. (2011) argued that North Brazil Current transport lags Labrador Sea convection in CM2.1 and is a useful indicator for AMOC variability. These two studies imply that freshwater fluxes likely play a role in generating AMOC variability. On the other hand, Frankcombe and Dijkstra (2009) argued that the dominant time scale of North Atlantic variability in CM2.1 is determined by the time for subsurface temperature anomalies to propagate westward as baroclinic Rossby waves.

Results from previous studies on CCSM3 and CM2.1 indicate that a number of factors may affect AMOC variability, and that there is no single underlying mechanism across models. The prevailing view appears to be that AMOC variability is excited by external NAO forcing in CCSM3 and freshwater fluxes in CM2.1. Thus far there has been little attempt to draw parallels between the two models and identify common driving mechanisms in them. This is the goal of the present study. We argue that, in both models, density anomalies are created in the subpolar gyre and affect AMOC via the thermal wind relation upon reaching the western boundary.

We begin by defining an index of MOC variability and go on to study how other aspects of the circulation, such as temperature T , salinity S , and potential density ρ anomalies, covary with it. Much use is made of composite property maps defined at various leads and lags referenced to a (HI) – (LO) MOC index, which is defined in section 2a. Emphasis is placed on density anomalies on the western margin of the gyre in the region of the

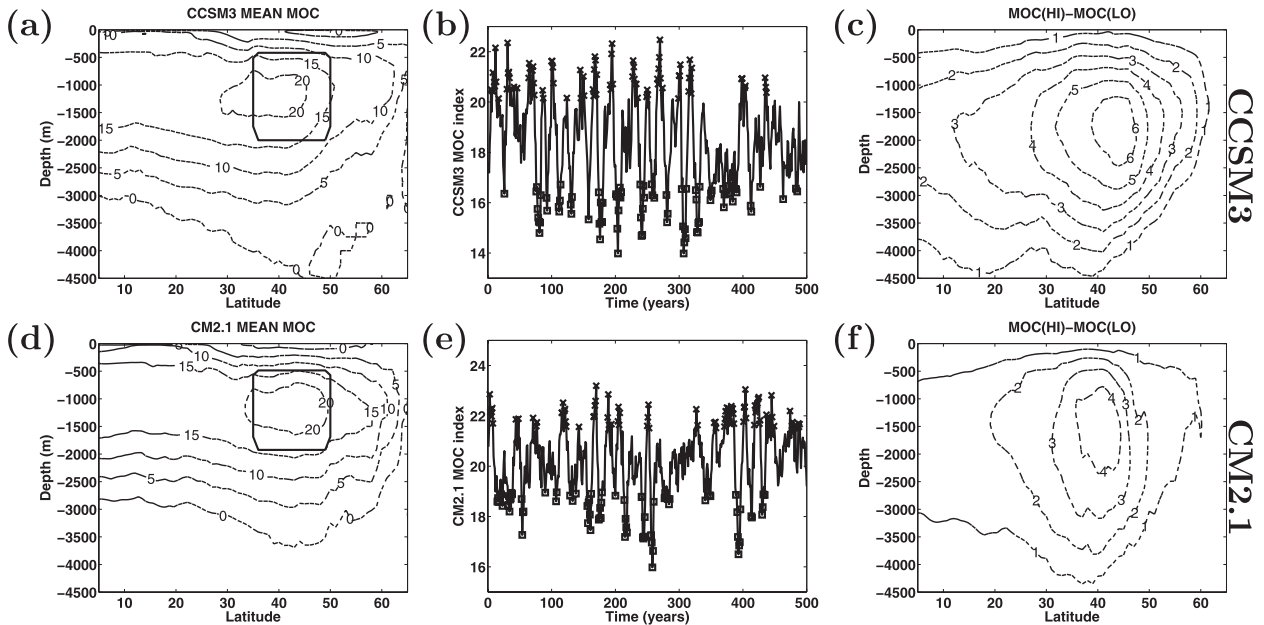


FIG. 1. (a) Eulerian-mean MOC (Sv) in the Atlantic in CCSM3 and (b) time series of the MOC index, defined as the average MOC from 35° to 50°N and from 1800- to 500-m depth, as indicated by the black box in (a). Years marked by times signs (squares) denote years that are more than one standard deviation above (below) the time mean. These are used to construct composite maps. (c) The MOC averaged over years marked by times signs minus the MOC averaged over years marked by squares, that is, the MOC(HI) – MOC(LO). The same variables are plotted for CM2.1 in (d),(e), and (f).

Grand Banks, which play a key role in pacing MOC variability in both models. We conclude the section by drawing together aspects of the variability that are common between the two models. This is used to motivate the construction of simplified toy models described in section 3.

a. MOC variability

Figures 1a,d show contours of the time averaged MOC [Sv ($1 \text{ Sv} \equiv 10^6 \text{ m}^3 \text{ s}^{-1}$)] in CCSM3 and CM2.1.¹ In both models the maximum overturning occurs just north of 40°N at a depth of roughly 1 km. Time series of annual-mean MOC averaged over the regions indicated by the black box (roughly from 35° to 50° and 1800- to 500-m depth) in each model are shown in Figs. 1b,e. Years that are more than one standard deviation above (below) the mean are marked with times signs (squares). These years will now be used to create composite variables based on a (HI) – (LO) MOC index, that is, composites are the average of a given variable over years when the MOC is

(HI) minus the average when the MOC is (LO). This technique was used, for example, in Czaja and Marshall (2001) to study the evolution of SST anomalies in the Atlantic based on an SST dipole index.

The (HI) – (LO) MOC pattern is shown in Figs. 1c,f. It has a maximum magnitude of 6.8 Sv in CCSM3 and 4.6 Sv in CM2.1 and is located near the black box at zero lag. The patterns are slightly deeper than the mean MOC, which is consistent with the first empirical orthogonal function (EOF1) see (Danabasoglu 2008).

b. Covarying temperature signals

Figures 2a,d show power spectra of the MOC indices (red lines) in Fig. 1 for both CCSM3 and CM2.1. Also plotted are power spectra of a temperature index T , defined as the upper 1-km temperature averaged over the gray-boxed region near the Grand Banks in Figs. 2b,c,e,f. The gray shading indicates 95% confidence limits of the MOC for a χ^2 distribution. The significance of this boxed region will become clearer in sections 2d and 2e below. In both models, peaks in variability are evident at approximately 20 years. Notice that the spectral content of the MOC index and the T index are very similar, indicating that the MOC and T indices are varying together, with perhaps a delay between them. The green lines show ω^{-2} power laws as follows: on sub-decadal time-scales the T signal is likely to be integrating

¹ Only the explicitly calculated, Eulerian component of the MOC is considered here, as in Danabasoglu (2008). In CM2.1, the parameterized bolus contribution has a negligible effect on the MOC spectrum since its variance is less than 1% of the Eulerian contribution.

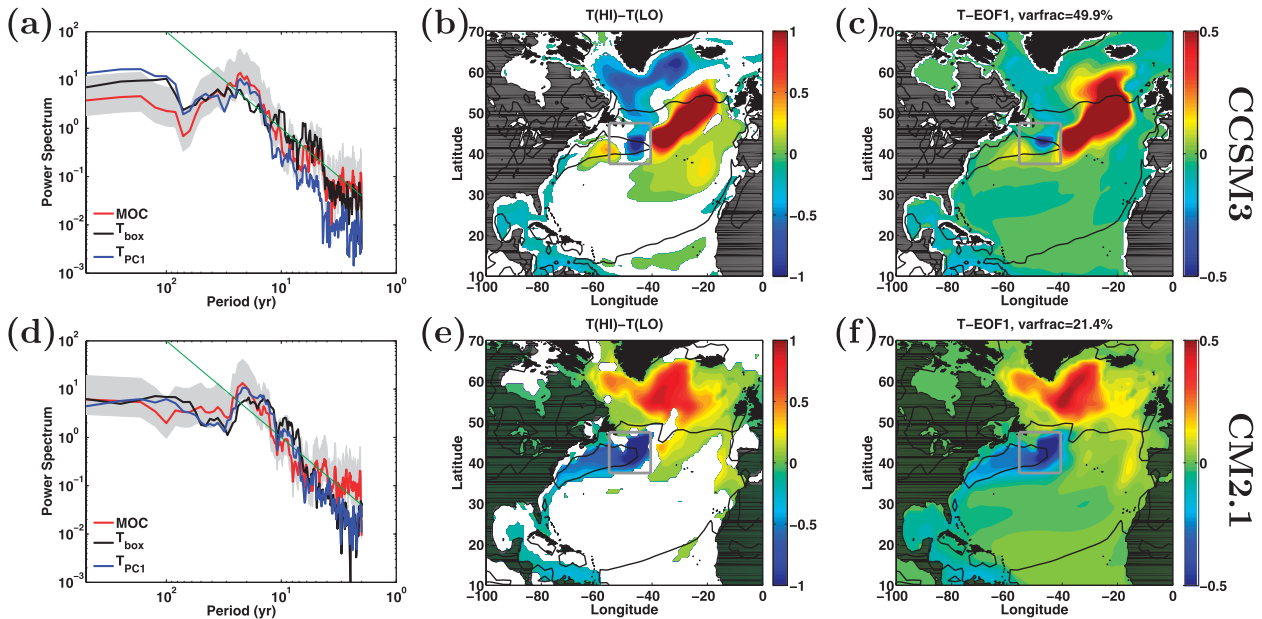


FIG. 2. (a) Normalized power spectra of the MOC index (red), temperature (K) averaged over the top 1 km in the gray-boxed regions [shown in (b),(c) (black)], and the first principal component of temperature (K) in the top 1 km (blue) in CCSM3. The green line indicates a -2 spectral slope, and the gray shading is a 95% confidence interval. (b) Composite (HI) – (LO) map of temperature averaged over the top 1 km, obtained by subtracting the low-index composite from the high-index composite, years marked by times signs and squares, respectively, in Fig. 1b. White shading indicates regions that are not significant at the 95% confidence level. (c) First EOF of temperature averaged over the top 1 km. The black contour indicates the time-mean 0-wind stress-curl line. (d),(e),(f) The same variables are plotted for CM2.1; see text for details.

a white noise process, consistent with Frankignoul and Müller (1979). Later, in section 3, we will model the decadal peak as a delayed oscillator using ideas in Marshall et al. (2001b).

Figures 2b,e show composite maps of T based on the (HI) – (LO) MOC index defined in Fig. 1. Regions where the (HI) – (LO) composites are not statistically significant at the 95% confidence level with the two-tailed Student's t test are shaded white. Note that the temporal degrees of freedom are estimated using effective sample size diagnostic of Bretherton et al. (1999). The spatial patterns of T at years with high MOC minus T in years with low MOC closely matches the EOF1 of T shown in Figs. 2c,f. Thus the primary mode of variability in T is nearly in phase with MOC. Cross-correlation analysis, not shown, reveals that (minus) the boxed T index lags MOC by 2 years in CCSM3, with cross correlation of about 0.47 (compared to a 95% confidence level of about 0.2), while in CM2.1 the T index is in phase with MOC with correlation 0.7 (compared to a 95% confidence level of about 0.185). As described in section 2f, the T -index delay in CCSM3 is likely due to deep convection in the Labrador Sea, which provides a slow pathway for subsurface density anomalies near 1-km depth to reach the Grand Banks region.

In both models, most of the variability of the MOC index is associated with temperature dominated density

anomalies on the western boundary near the Grand Banks, that is, the blue regions within the gray boxes in Fig. 2, which will be described in more detail in section 2d. The black contours in Figs. 2b,c,e,f indicate the time-mean zero wind stress curl lines, roughly marking the gyre boundaries. The close correspondence between the maximum temperature variations and the zero-wind stress curl line is indicative of a possible role of wind forcing because the greatest part of the wind stress curl variability lies near the zero wind stress curl line.

c. Covarying density signals

Figure 3 shows composite maps of potential density averaged over the top 1 km using the (HI) – (LO) MOC index in CCSM3. Figure 3b is computed by subtracting the high-index composite from the low-index composite. The (HI) – (LO) map in Fig. 3b is very similar to the map in Fig. 2b (but with opposite sign), indicating that density anomalies at high and low MOC states are dominated by temperature anomalies. The corresponding (HI) – (LO) salt map (not shown) has very similar patterns and signs as Fig. 2b, showing that T and S are compensated, except in the Labrador Sea region (as noted by Danabasoglu 2008). The most pronounced feature of the density pattern (blue region in Fig. 3b) forms near the zero wind stress curl line and the mid-Atlantic ridge. The

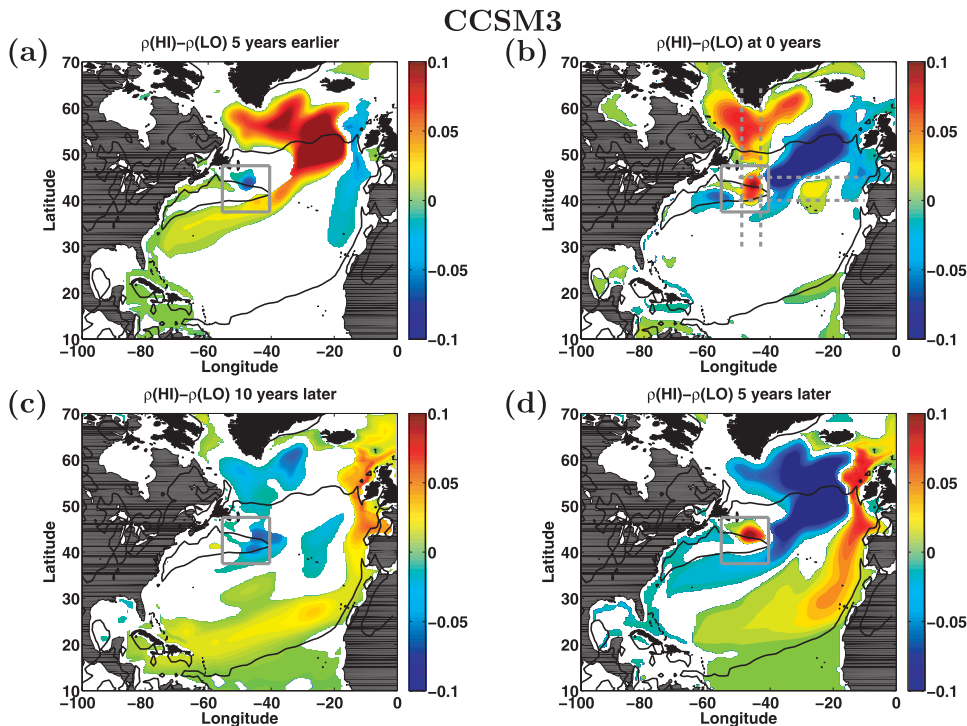


FIG. 3. Composite maps of potential density (kg m^{-3}) averaged over the top 1 km using the index described in Fig. 2 for CCSM3. (a) The 5-years-earlier map is obtained by subtracting the (low index – 5 years) composite from the (high index – 5 years) composite. (b) As in (a), but at the composite index years; (d) as in (a), but 5 years after the composite years; and (c) as in (a), but 10 years after the composite years. Thus, the anomalies evolve in time from the top left to the bottom left. White shading indicates regions that are not significant at the 95% confidence level. The dashed gray lines in (b) denote sections plotted in Fig. 5, below.

“5 years earlier” map in Fig. 3a is obtained by taking the average of (HI – 5) years minus the average of (LO – 5) years. It shows advection of a positive density anomaly around the subpolar gyre. The “5 years later” map in Fig. 3d shows the opposite phase, with a negative density anomaly beginning to advect cyclonically around the subpolar gyre. Also, the positive density anomaly that previously propagated around the subpolar gyre has merged with another positive density anomaly that formed in situ off of the Grand Banks (i.e., inside the boxed region in Fig. 3b). This merging of positive density anomalies is also visible in the meridional section shown in Fig. 5c. Labrador Sea anomalies subduct and propagate southward before merging with a shallower density anomaly in the Grand Banks region.

Figure 4 shows maps of potential density based on the composite (HI) – (LO) MOC index in CM2.1, analogous to Fig. 3 for CCSM3. In CM2.1, as in CCSM3, the composite density map at 0 years (Fig. 4b) closely matches the composite temperature map in Fig. 2d: temperature dominates, with salinity compensating (not shown) everywhere except in the region of deep convection in the Labrador Sea, where salt anomalies dominate

at 0 lag. Again, the largest density anomalies are found along the zero wind stress curl line, but they originate farther north near the mid-Atlantic ridge and propagate both west into the Labrador Sea and southwest into the region off the Grand Banks.

d. Role of density anomalies on the western boundary

Buckley et al. (2012) showed that MOC variability occurs almost entirely on the western boundary in coupled aqua-planet simulations with meridional continental barriers. In one of their model configurations, with flat bottom bathymetry, anomalies generated near the eastern boundary propagate westward and trigger MOC variations when they reach the western boundary, in accord with the thermal wind relation. The temperature anomalies shown in Fig. 2 form in different locations in the two more realistic models studied here, but all models suggest that density anomalies propagate around the subpolar gyre and influence the MOC when they reach the western boundary.

Here, motivated by that study, we investigate the role of density anomalies on the western boundary and their

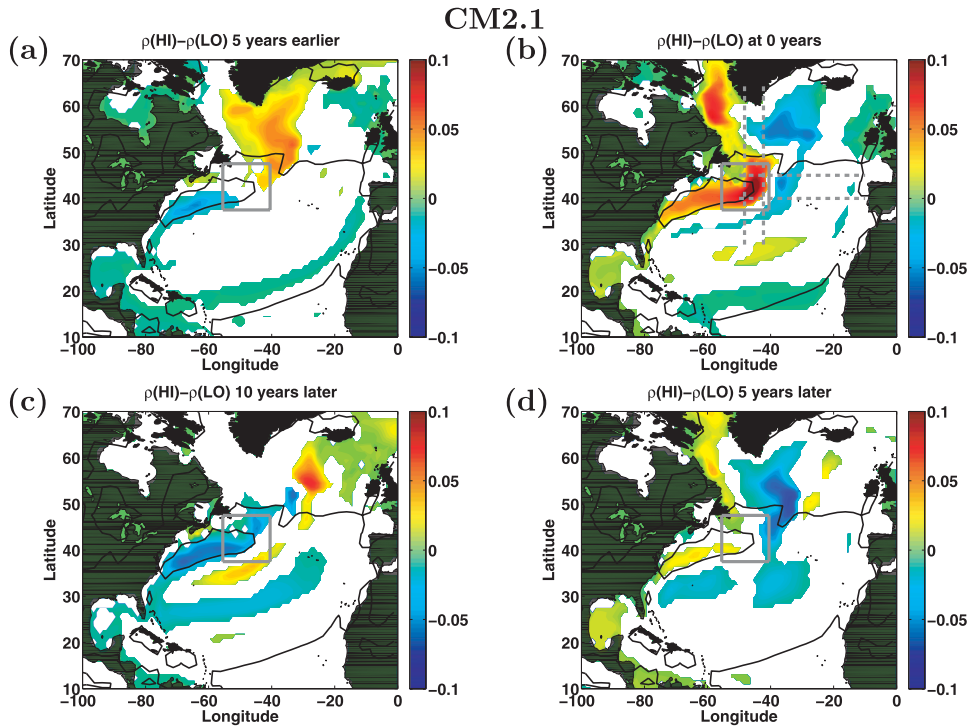


FIG. 4. As in Fig. 3, but for CM2.1.

association with MOC anomalies. Figure 5 shows composites of zonal and meridional cross sections of meridional velocity and density in CCSM3 (top row) and CM2.1 (bottom row), from the regions indicated by the gray dashed lines in Figs. 3d and 4d. The zonal cross sections are averaged from 40° to 45°N, which is approximately the latitude range where the MOC is largest. The meridional cross sections are averaged from 50° to 40°W, encompassing the longitude where the deep western boundary current flows offshore of the Grand Banks and where density anomalies associated with MOC variability are found. Figure 5a shows that the largest transport differences between high and low MOC years occurs around 40°W, where both the Gulf Stream and the deep western boundary current are anomalously strong. The tripole pattern of meridional velocity in Fig. 5a is consistent with the density dipole present in the zonal section of Fig. 5b. However, as is evident from a consideration of the thermal wind equation (see below) the positive density anomaly on the western boundary is associated with the major part of MOC variability.

The bottom row of Fig. 5 shows zonal and meridional composite cross sections of meridional velocity and density in CM2.1, averaged over the same latitude and longitude bands. Analogously to CCSM3, the transport anomalies in Fig. 5d are centered over 40°W and are a maximum when the Gulf Stream and deep western boundary current are

strong. Again, there is also a clear positive density anomaly on the western boundary in Fig. 5e.

The anomalous meridional transport can be related to zonal density gradients through the thermal wind relation (Hirschi and Marotzke 2007):

$$f \frac{\partial v}{\partial z} = -\frac{g}{\rho_0} \frac{\partial \rho}{\partial x};$$

thus,

$$\bar{v}^x(z') = \int_{x_w}^{x_E} v dx = \frac{g}{\rho_0 f} \int_{-H}^{z'} \rho(\text{WB}) - \rho(\text{EB}) dz, \quad (1)$$

where ρ_0 is the mean density, f is the Coriolis parameter, g is the acceleration due to gravity, and $\rho(\text{WB})$ and $\rho(\text{EB})$ are the density anomalies on the western and eastern boundaries. On integrating vertically we obtain an anomalous overturning streamfunction of

$$\psi_\rho(z) \approx - \int_{-H}^z \left[\bar{v}^x(z') - \frac{1}{H} \int_{-H}^0 \bar{v}^x dz' \right] dz', \quad (2)$$

where the vertical average of \bar{v}^x has been subtracted out to ensure that $\psi_\rho(z=0) = \psi_\rho(z=-H) = 0$.

In Fig. 6 we compare the MOC variability MOC(HI) – MOC(LO) (solid lines) with the anomalous transport computed from the density anomalies on the western boundary $\psi_\rho(\text{WB})$ (dashed lines) in the two models. The

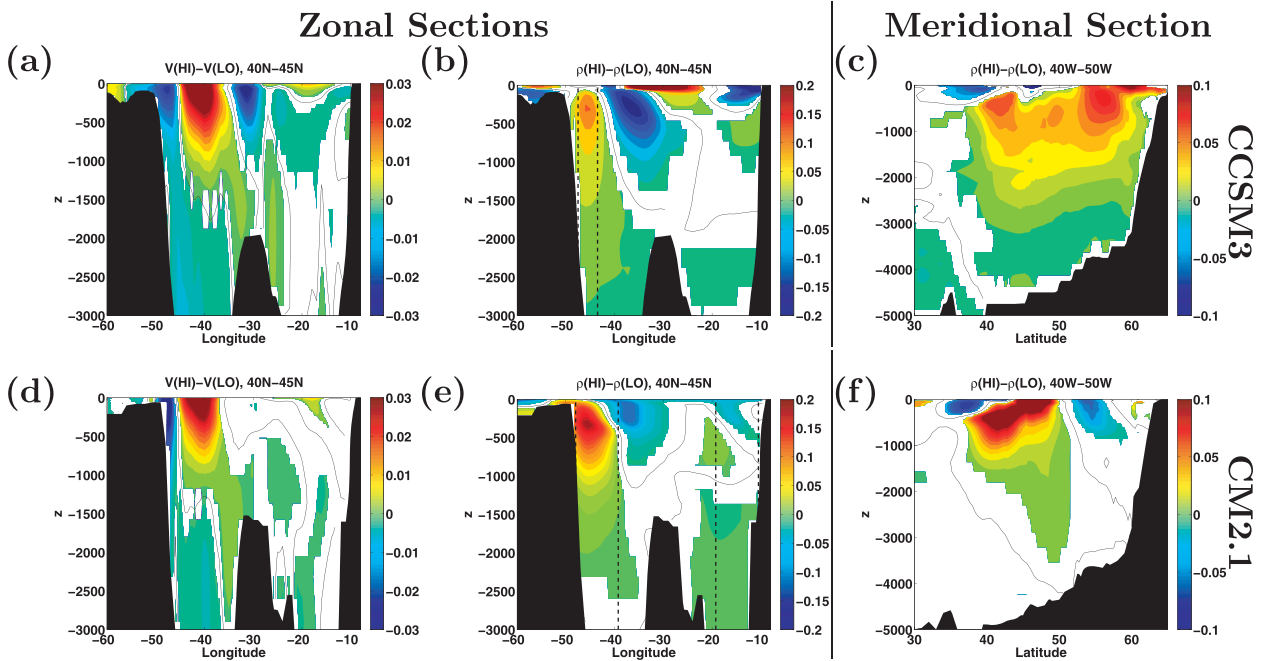


FIG. 5. Composite zonal and meridional cross sections of meridional velocity (m s^{-1}) and density (kg m^{-3}) in (top) CCSM3 and (bottom) CM2.1. The zonal cross section is averaged from 40° to 45°N , and the meridional cross section is averaged from 40° to 50°W (land points were excluded from the zonal mean). Dashed lines in (b) and (e) indicate the extent away from the shelf that ρ was averaged over to compute ρ_{WB} and ρ_{EB} (the contribution of ρ_{EB} in CCSM3 was negligible because $\int_H^0 \rho dz \approx 0$) in Fig. 6. White shading indicates regions that are not significant at the 95% confidence level.

contribution of density anomalies on the eastern boundary $\psi_\rho(\text{EB})$ is negligible in CCSM3 and is much smaller than $\psi_\rho(\text{WB})$ in CM2.1 (as indicated in Fig. 6b). The MOC variability $\text{MOC}(\text{HI}) - \text{MOC}(\text{LO})$ is defined as the average MOC in “high” years minus the average MOC in “low” years averaged from 40° to 45°N , while $\psi_\rho(\text{WB})$ is computed using Eq. (2) applied to the density fields shown in Figs. 5b,e. The dashed lines in Figs. 5b,e indicate regions over which density was zonally averaged to estimate $\psi_\rho(\text{WB})$, that is from the shelf out to the dashed line.

The close match between $\text{MOC}(\text{HI}) - \text{MOC}(\text{LO})$ and $\psi_\rho(\text{WB})$ in both models is perhaps not unexpected in view of the thermal wind equation. As noted above, this is also a property of the coupled, idealized models studied in Buckley et al. (2012). It highlights the close association between density anomalies on the western boundary and MOC variability. Understanding how those density anomalies are created, how they arrive at the western boundary, and what sets their time scale of variability, is key to understanding how the MOC varies.

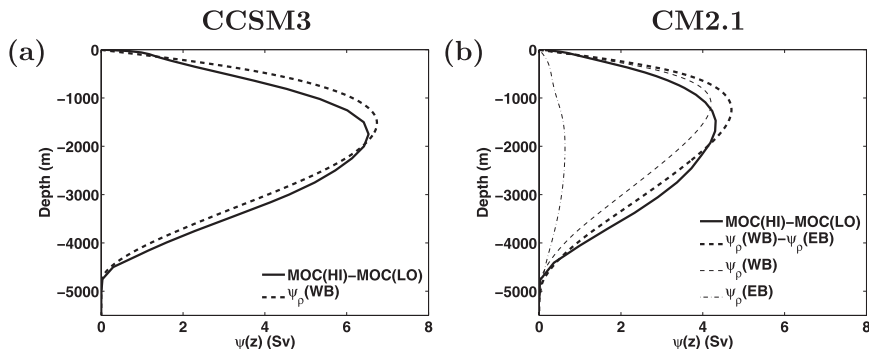


FIG. 6. (HI) – (LO) index composite mean MOC averaged from 40° to 45°N (solid lines) and anomalous streamfunction computed from the composite zonal cross sections of density (dashed lines) in Figs. 5b,e using Eq. (2). Note that density anomalies on the eastern boundary are negligible in CCSM3. See text for details.

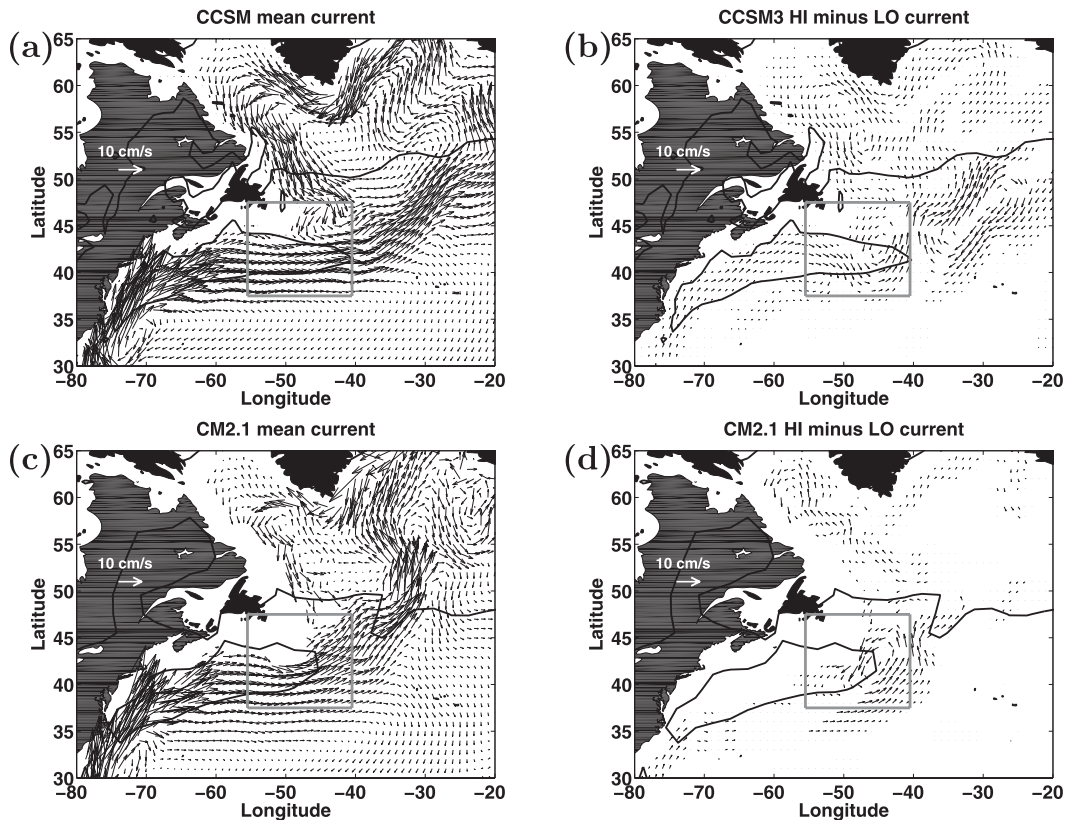


FIG. 7. (a) Mean velocity and (b) composite maps of velocity using the index described in Fig. 2 near 300 m (layer 17) in CCSM3. (c) Mean velocity and (d) composites near 300 m (layer 27) in CM2.1. Only vectors significant at the 95% confidence level are shown.

e. Role of the Mann eddy

As shown in Figs. 2–4, MOC variability is associated with upper-ocean, temperature-dominated density anomalies at the western boundary near the Grand Banks. Figure 7 shows mean currents and (HI) – (LO) composites at 300-m depth in the two models. The (HI) – (LO) composites of each model reveal that in association with a strong MOC there is anomalously cyclonic circulation in the boxed region and a somewhat enhanced Gulf Stream and Labrador Current. These cyclonic anomalies are in geostrophic balance with the positive buoyancy anomalies shown in Figs. 3b and 4b. We believe it is significant that these cyclonic anomalies are at the location of the respective model's representation of the Mann eddy. In the ocean, the Mann eddy is a persistent anticyclone swirling at the end of the separated Gulf Stream to the southeast of the NAC, located approximately between 38° and 45°N and between 40° and 50°W (Mann 1967; Meinen et al. 2000). This is the region where the deep expression of the southward-flowing Labrador Current abuts the northward-flowing Gulf Stream. The variability of the Mann Eddy likely modulates the trajectory of the

NAC and the strength of the MOC. We hypothesize that the cyclonic circulation within the boxed regions of the (HI) – (LO) composites in Figs. 7b,d imply that a weakened Mann eddy is associated with an enhanced MOC.

f. Role of Labrador Sea convection

In CCSM3, there is a clear connection between density anomalies that propagate around the subpolar gyre, precondition convection, and result in density anomalies that later appear in the 40°–45°N latitude band (see Fig. 5b). Figure 8a shows (HI) – (LO) composite maps of March mixed layer depth (MLD). The first EOF of MLD variability shown in Fig. 8b is very similar to the (HI) – (LO) composite maps. Cross correlations of T , S , ρ (at 150-m depth in the box in the region of maximum MLD variability) against MLD (in the same box) and the MOC index defined in Fig. 1 are shown in Figs. 8c,d. Density anomalies are in phase with the MLD anomalies and so it seems clear that the propagation of density around the subpolar gyre is preconditioning Labrador Sea deep convection—see the review in Marshall and Schott (1999). Figure 8d shows that density anomalies in the Labrador Sea region lead MOC anomalies (see also

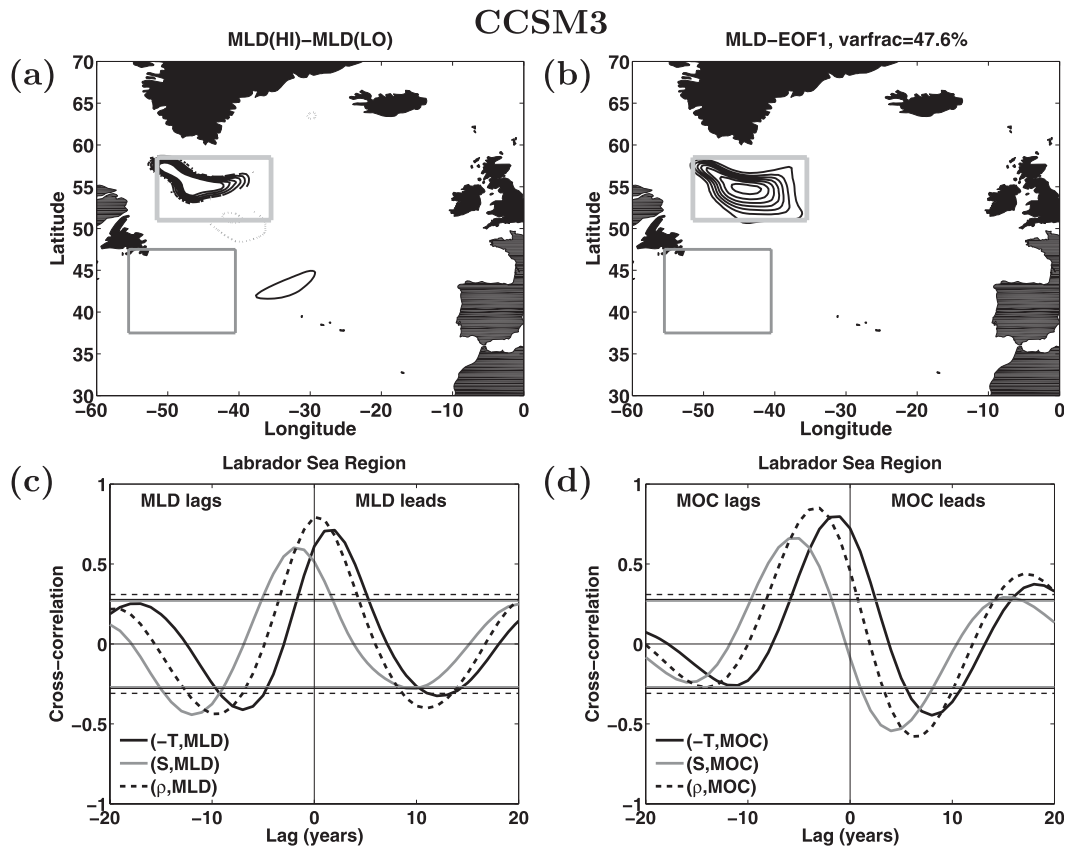


FIG. 8. (a) Contours of March mixed layer depth (m) in CCSM3 using the index described in Fig. 2. Thick solid contours are 100–700 m spaced by 100 m, while gray-dotted contours show -100 and -200 m and a thin solid contour shows 0 m. (b) Contours from 100 to 700 m of the first EOF of March mixed layer depth in CCSM3 with thick gray box indicating Labrador Sea Region for box averaging. (c) Cross correlation between T , S , and ρ against mixed layer depth in the thick boxed region shown in the Labrador Sea in (a),(b). (d) Cross correlation between T , S , and ρ in the Labrador Sea Region against the MOC index defined in Fig. 1.

Danabasoglu 2008). The propagation of deep density anomalies from the Labrador Sea to the region of maximum MOC can be seen coming from north of 50° in Fig. 5c. However, a significant fraction of the density anomaly at 42°N does not originate in the Labrador Sea.

In CM2.1, the connection between MOC variability and deep convection in the Labrador Sea is less clear. The principle component time series of EOF1 of MLD does covary with MOC index, however, its spatial pattern is a large dipole covering the Labrador Sea region (not shown). Consequently, cross correlations between (T , S , and ρ) in the Labrador Sea (northernmost boxed region shown in Fig. 8) and the maximum MOC (i.e., the index defined in Fig. 1) are insignificant. Similarly, cross correlations between (T , S , and ρ) and MLD are not significant since the northern box overlaps the EOF1 dipole. Figure 5f also indicates that MOC variability is mainly due to near-surface density anomalies south of 50°N , with little indication of a role for convection north of 50°N .

In summary, Labrador Sea convection does seem to play a role in creating density anomalies off Georges Bank in CCSM3, but there is little evidence that it is creating density anomalies there in CM2.1. In both models density anomalies off Georges Bank set the strength of the MOC through thermal wind, and are controlled by the advection of density anomalies around the subpolar gyre.

3. Idealized toy model of MOC variability

a. Construction of an “oscillator model”

In the previous section we showed that MOC variability covaries with temperature-dominated density anomalies on the western boundary of the subpolar gyre. The dominant time scale of the variability appears to depend on the time it takes for the density anomalies to propagate around the subpolar gyre and reach the western boundary. We hypothesize, as do Kwon and Frankignoul (2012) and Danabasoglu (2008), that such anomalies could

be energized by stochastic atmospheric forcing. In this section we apply the ideas of Marshall et al. (2001b) to formulate a delayed oscillator toy model of the MOC variability. This is a modification of the canonical model of the interaction of ocean with the atmosphere due to Frankignoul and Hasselmann (1977, hereafter referred to as FH77):

$$\frac{\partial T}{\partial t} = \mathcal{F} - \lambda T, \quad (3)$$

where T denotes a near-surface temperature (FH77 assumed it to be SST), λ is a damping time scale (of order of a season), and \mathcal{F} is the surface forcing (Ekman pumping and turbulent heat flux) associated with atmospheric variability. In FH77 \mathcal{F} is taken to be a white noise process, so that Eq. (3) predicts a red spectrum for T on time scales shorter than λ^{-1} and a flattening on longer time scales. This is obviously not a good model of the processes that lead to the spectra shown in Fig. 2, which exhibit a pronounced spectral peak at (see below) roughly the time it takes a baroclinic Rossby wave to propagate across the basin.

We therefore make use of a simple elaboration of Eq. (3), which is capable of capturing a spectral peak through a delayed oceanic response of T to external meteorological forcing. Accordingly we modify Eq. (3) with a delay term, D , thus, to represent ocean circulation:

$$\frac{\partial T}{\partial t} = -\tau - \lambda T - DT(t - t_d), \quad (4)$$

where

$$\tau = \alpha \mathcal{N} - fT. \quad (5)$$

In our interpretation of Eq. (4), T denotes the strength of upper-ocean thermal anomalies on the western boundary (for example in the box in Fig. 7), τ is the amplitude of the wind stress variability (in temperature units) blowing over the basin that is assumed to be decomposed into a stochastic component \mathcal{N} and, possibly, an SST-induced feedback component (fT). Key model parameters are as follows [they are discussed in much more detail in Marshall et al. (2001b)]:

- α —scaling of stochastic wind stress \mathcal{N} into a temperature tendency,
- λ —damping due to air–sea interaction,
- f —feedback of T on the wind stress pattern, and
- D and t_d —measure the strength and time-delay of the feedback of ocean circulation on T .

We present the delay term in Eq. (4) as a representation of advective and wave ocean processes that, on long

time scales, play a role in setting T . Clearly it is a highly symbolic characterization of the processes at work in the ocean and ocean models. However, it should be noted that, as shown in Marshall et al. (2001b), a term of this form arises from a consideration of time-dependent Sverdrup dynamics and thermohaline circulation dynamics. Here we are agnostic as to the detailed processes that control D and t_d and, instead, adjust these model parameters to best-fit model spectra.

For $f = 0$, the solution to Eq. (4) in the Fourier domain is given by

$$\hat{T} = -\frac{\alpha \hat{\mathcal{N}}}{i\omega + De^{-i\omega t_d} + \lambda}, \quad (6)$$

where $|\hat{\mathcal{N}}|^2 = 1$, and $T(t) = \int \hat{T}(\omega) e^{i\omega t} d\omega$. Figure 9 shows the spectra (Fig. 9a) and “free solutions” (Fig. 9b) for $D = 0, 0.1, 0.2$, and 0.3 yr^{-1} with $\alpha = 1 \text{ K m}^2 \text{ N}^{-1}$, $t_d = 8 \text{ yr}$, and $\lambda = 2\pi/32 \text{ yr}^{-1}$, as in Plate 1 of Czaja and Marshall (2000). The free (or unforced) solutions are obtained by setting $\alpha = 0$, initializing with a cosine function for $t < 0$, and then allowing them to decay away in time, thus

$$T_{\text{free}} \propto e^{-\gamma t/2} \cos(\omega_0 t), \quad (7)$$

where ω_0 measures the frequency of the oscillation and γ the decay rate. The parameter γ in Eq. (7) is obtained by a least squares fit over the first few oscillations of the free solutions. Decay rates in Fig. 9 are $\gamma = 2\pi/16, 2\pi/13.5, 2\pi/29.5$, and $2\pi/132.5 \text{ (yr)}^{-1}$ for $D = 0, 0.1, 0.2$, and 0.3 (yr)^{-1} , respectively. From these decay rates and ω_0 we can define a Q-factor:

$$q = \frac{\omega_0}{\gamma}. \quad (8)$$

The Q-factor measures the number of distinct oscillations and is approximately 0, 1, 2.5, and 11.5 in the four cases. The Q-factor can also be measured directly from the spectral density of T as the peak frequency divided by the bandwidth of the range of frequencies for which the energy is half its peak value.

b. Fitting the oscillator model to the “observed” spectra

To fit the delayed oscillator model to observed spectra it is useful to consider two extreme frequency limits implied by Eq. (6) as follows:

$$\lim_{\omega \rightarrow 0} |\hat{T}|^2 = \left(\frac{\alpha}{D + \lambda} \right)^2 \quad \text{and} \quad (9)$$

$$\lim_{\omega \rightarrow \infty} |\hat{T}|^2 = \frac{\alpha^2}{\omega^2}. \quad (10)$$

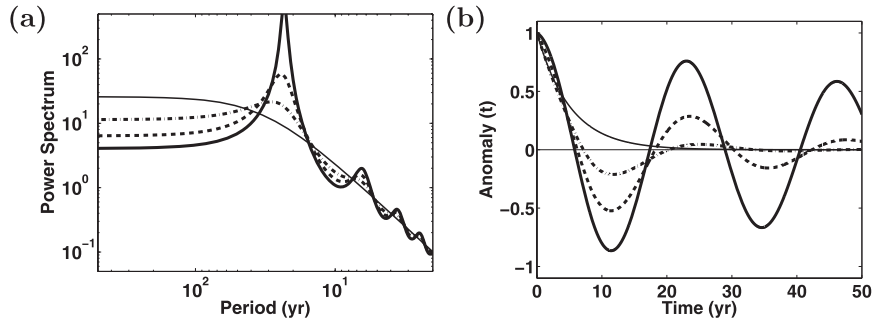


FIG. 9. (a) Spectra predicted by the delayed oscillator model in Eq. (4) with parameters $\alpha = 1$, $t_d = 8$ yr, $\lambda = 2\pi/32$ yr $^{-1}$, $D = 0$ (thin solid line), $D = 0.1$ (dash-dotted, $q \approx 1$), $D = 0.2$ (dashed, $q \approx 2.5$), and $D = 0.3$ (thick solid line, $q \approx 11$). (b) Free solutions to Eq. (4) as in Czaja and Marshall (2000), see text for details.

We first solve for α in the $\omega \rightarrow \infty$ limit, then solve for $D + \lambda$ using the $\omega \rightarrow 0$ limit. Note that the time delay t_d is tightly constrained by the frequency of the spectral peak because resonance occurs when $\omega t_d = \pi/2$, giving an oscillation period of $4t_d$ in the absence of damping (i.e., $\lambda = 0$). Also note that D determines the height of the spectral peak, and λ acts as a limiter on growth toward low frequencies.

Figures 10a,b show normalized spectra (blue curves) for CCSM3 and CM2.1 and the reconstructed spectra using a purely statistical autoregressive (AR $_{15}$) least squares fit (black curves) and the delayed oscillator model in Eq. (4) (red curves) fitted manually using the statistical fit as a guide.² The fitted delayed oscillator parameters in CCSM3 are

- $\alpha = 0.6$, $t_d = 7$ yr, $D = 0.17$ yr $^{-1}$, and $\lambda = 0.157$ yr $^{-1}$, while in CM2.1 they are
- $\alpha = 0.4$, $t_d = 5$ yr, $D = 0.2$ yr $^{-1}$, and $\lambda = 0.063$ yr $^{-1}$.

From these parameters we can deduce ω_0 and γ in Eq. (7) and then compute the Q-factor in CCSM3:

- $\omega_0 = 2\pi/24$ yr $^{-1}$, $\gamma = 2\pi/43$ yr $^{-1} \Rightarrow q = 1.8$,

and for CM2.1

- $\omega_0 = 2\pi/21.5$ yr $^{-1}$, $\gamma = 2\pi/38$ yr $^{-1} \Rightarrow q = 1.76$.

We note in passing that these fitted delay times t_d are broadly consistent with the transit time of Rossby waves in the North Atlantic at 40°N. Using data from Tulloch et al. (2009), we estimate the observed Rossby wave phase speed in the eastern Atlantic to be about 2 cm s $^{-1}$

from 40° to 50°N, which gives transit times on the order of 5–10 years. Also, as pointed out by Kwon and Frankignoul (2012), the regime from years 51 to 350 in CCSM are more predictable than all of the years. We estimate the Q-factor for this range of years to be about $q = 3$.

c. Implications for predictability

The delayed oscillator models fit the spectral peak, some of the higher harmonics, and the low frequencies quite well, indicating that they can perhaps be used to make predictions. Here we show a sample prediction from such a fitted toy model and compare it with a purely statistical prediction, assuming perfect initial conditions. We simply train our toy model on the MOC time series, but bear in mind that a real prediction would require training our model against a subsurface temperature fingerprint, as done in Mahajan et al. (2011b).

Figures 10c,d show ensemble mean predictions in CCSM3 and CM2.1 with the model parameters given above. To create the predictions, ensembles for the statistical and delayed oscillator models were initialized with the MOC from the 15 years preceding the starting year, which is denoted in the figure by vertical dashed lines. As time progresses, the ensemble means decay away because the ensemble members become uncorrelated. The predictions shown here are the ensemble means scaled by those decay rates ensuring that the magnitudes of the predictions remain roughly constant in time. Both the statistical (AR $_{15}$) and delayed oscillator predictions track the MOC for a couple of oscillations before losing the phase, consistent with Q-factors of about 2. As expected from their power spectra, the statistical and delayed oscillator predictions are almost identical for the first couple of cycles and then diverge as either fast time-scale errors accumulate or long time-scale errors start to appear. However, the quality of the predictions depends on how

² Our delayed oscillator model has only three free parameters, yet it is compared to a higher-order autoregressive model here.

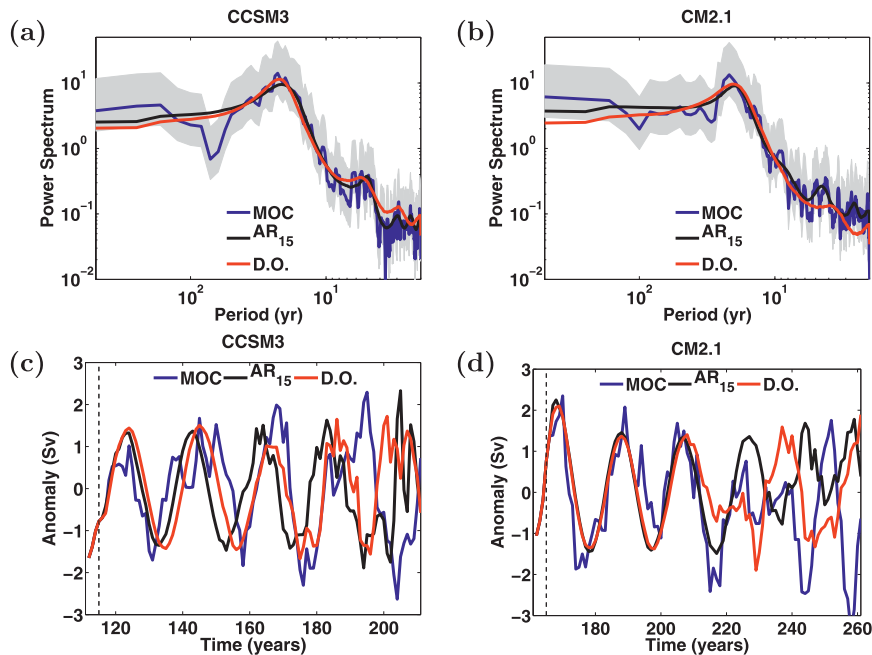


FIG. 10. Fit of delayed oscillator models (red lines) to the MOC spectra (blue lines) in (a) CCSM3 and (b) CM2.1. Also plotted in black are spectra of autoregressive (AR_{15}) fits to the MOC. (c),(d) Example predictions for the two models are shown.

representative the predicted years are to the average behavior over the 500-yr time series. Note that the predictions shown in Fig. 10 correspond to instances where the prediction tracks MOC longer than suggested by the model's Q-factors. Other initial conditions result in predictions which lose the phase of the MOC within a few years.

Our results are broadly in accord with those of Mahajan et al. (2011b), who attempted to predict AMOC variations using an autoregressive model (AR_2) tuned to the subsurface temperature anomalies, or “AMOC fingerprints,” defined in Zhang (2008). They predicted a drop in AMOC strength in the few years following its peak in 2005. This was based on the fidelity of their AR_2 model in hindcasts of observed subsurface temperature anomalies and the close connection between AMOC variability and subsurface temperature variability in CM2.1. Mahajan et al. (2011b) also found that hindcasts from their AR_2 model show comparable skill whether they are trained on 500 years or only 50 years of CM2.1 data, although they note that the 20-yr spectral peak in CM2.1 is not robust across models or the observations. Msadek et al. (2010) also argued that AMOC in CM2.1 is predictable for up to 20 years.

4. Summary and discussion

By using the same diagnostic tools to study variability in two coupled climate models, we have identified

aspects that are common to them both. In particular we find the following:

- (i) AMOC variability is associated with upper ocean (top 500 m to 1 km) density anomalies on the western margin of the basin in the region of the Mann eddy. These anomalies modulate the trajectory and strength of the NAC. The importance of the western margin is a direct consequence of the thermal wind relation and is independent of the mechanism that creates those density anomalies.
- (ii) Density anomalies in this key region are part of a larger-scale density pattern that propagates around the subpolar gyre. These act as a “pacemaker” of AMOC variability.
- (iii) Density anomalies are dominated by temperature, with salinity playing a lesser role.
- (iv) The time scale of AMOC variability is broadly consistent with the inherent time scale set by the transit time of first baroclinic mode Rossby waves at 45°N (not shown).
- (v) Although we are unable to identify how the density anomalies are created, they appear to emanate along the zero-wind stress curl line separating the subtropical and subpolar gyres. It is here that modeled (NAO) wind variability is a maximum. We suspect that this external wind forcing gives rise to thermocline undulations as in Frankignoul et al. (1997) that, when they strike the western boundary, spin up the

AMOC. A hierarchy of ocean-only and coupled experiments would be required to confirm or reject this conjecture.

- (vi) Density anomalies entering regions of deep convection (e.g., the Labrador Sea) can act to precondition convection. This is clearly evident in CCSM3 but less important in CM2.1. Deep, convectively formed anomalies can then propagate southward on the western boundary current to the region of the Mann eddy and thence induce changes in the AMOC.
- (vii) Fitting a delayed oscillator model to the spectra found in the two models suggests that AMOC variability has a Q-factor of around 2, implying predictability out to a couple of cycles or so. This can be used as a minimalist model against which more complex predictability systems can be compared.

Finally, it should be noted that an association between MOC variability and density anomalies on the western margin of the gyre (offshore of the Grand Banks in the region of the Mann eddy) is, in retrospect, not surprising. Zonal and vertical integration of the thermal wind equation links changes in geostrophic contributions to MOC to those of depth integrated buoyancy differences between the zonal endpoints. To the extent that anomalies on the eastern boundary are much smaller than anomalies on the west, anomalies on the west become the dominant contributor to MOC variability on decadal time scales. This could explain why, for example, MOC variability is so sensitive to model formulation, both between models and in the same model when changes are made to its resolution overflow parameterizations, etc. For example Danabasoglu et al. (2012) and Yeager and Danabasoglu (2012) describe AMOC variability in CCSM4 and find significant sensitivity to how Nordic Sea overflows are parameterized. The dynamics of the ocean in the region of the Mann eddy is a “crossroad” where potential vorticity anomalies created in distant parts of the basin are brought together and interact. This is indeed a very complex region and will be sensitive to model resolution and parameterization.

Acknowledgments. This study is part of a collaborative project among MIT, GFDL, and NCAR supported from Jim Todd’s NOAA CLIVAR program. Ross Tulloch is supported as a NOAA postdoctoral fellow. We thank David Ferreira and Martha Buckley for helpful discussions. Thanks also are given to Tom Delworth (GFDL) and Gokhan Danabasoglu (NCAR) for making available their model results and their openness in discussing them.

APPENDIX

Climate Models

The NCAR CCSM3 coupled model is described in detail in Danabasoglu (2008). It uses the Community Atmosphere Model, version 3 (CAM3), the Community Land Model, version 3 (CLM3), the Parallel Ocean Program, version 1.4 (POP1.4), and the Community Sea Ice Model (CSIM). The atmospheric model is at T85 resolution with 26 vertical levels, and the ocean model has nominal 1° horizontal resolution and 40 vertical levels. Here we analyze years 101–600 of the 700-yr present-day (1990) control integration experiment b30.009.

The GFDL 2.1 coupled model, described in Delworth et al. (2006), has $2.5^\circ \times 2^\circ$ horizontal resolution and 24 vertical levels in the atmosphere and uses the Modular Ocean Model, version 4 (MOM4), which has nominal 1° horizontal resolution and 50 vertical levels. Here we analyze years 1–500 of the preindustrial (1860) control experiment 1860-D4.

REFERENCES

- Bretherton, C. S., M. Widmann, V. P. Dymnikov, J. M. Wallace, and I. Blade, 1999: The effective number of spatial degrees of freedom of a time-varying field. *J. Climate*, **12**, 1990–2009.
- Buckley, M. W., D. Ferreira, J.-M. Campin, J. Marshall, and R. Tulloch, 2012: On the relationship between decadal buoyancy anomalies and variability of the Atlantic meridional overturning circulation. *J. Climate*, in press.
- Colin de Verdière, A., and T. Huck, 1999: Baroclinic instability: An oceanic wavemaker for interdecadal variability. *J. Phys. Oceanogr.*, **29**, 893–910.
- Czaja, A., and J. C. Marshall, 2000: On the interpretation of AGCMs response to prescribed time-varying SST anomalies. *Geophys. Res. Lett.*, **27**, 1927–1930.
- , and —, 2001: Observations of atmosphere–ocean coupling in the North Atlantic. *Quart. J. Roy. Meteor. Soc.*, **127**, 1893–1916.
- Dai, A., A. Hu, G. A. Meehl, W. M. Washington, and W. G. Strand, 2005: Atlantic thermohaline circulation in a coupled general circulation model: Unforced variations versus forced changes. *J. Climate*, **18**, 3270–3293.
- Danabasoglu, G., 2008: On multidecadal variability of the meridional overturning circulation in the Community Climate System Model, version 3. *J. Climate*, **21**, 5524–5544.
- , S. G. Yeager, Y.-O. Kwon, J. J. Tribbia, A. Phillips, and J. Hurrell, 2012: Variability of the Atlantic meridional overturning circulation in CCSM4. *J. Climate*, in press.
- Delworth, T., and R. J. Greatbatch, 2000: Multidecadal thermohaline circulation variability driven by atmospheric surface flux forcing. *J. Climate*, **13**, 1481–1495.
- , and M. E. Mann, 2000: Observed and simulated multidecadal variability in the Northern Hemisphere. *Climate Dyn.*, **16**, 661–676.
- , S. Manabe, and R. J. Stouffer, 1993: Interdecadal variations of the thermohaline circulation in a coupled ocean–atmosphere model. *J. Climate*, **6**, 1993–2011.

- , —, and —, 1997: Multidecadal climate variability in the Greenland Sea and surrounding regions: A coupled model simulation. *Geophys. Res. Lett.*, **24**, 257–260.
- , and Coauthors, 2006: GFDL's CM2 global coupled climate models. Part I: Formulation and simulation characteristics. *J. Climate*, **19**, 643–674.
- Dong, B., and R. T. Sutton, 2005: Mechanism of interdecadal thermohaline circulation variability in a coupled ocean–atmosphere GCM. *J. Climate*, **18**, 1117–1135.
- Eden, C., and J. Willebrand, 2001: Mechanism of interannual to decadal variability of the North Atlantic circulation. *J. Climate*, **14**, 2266–2280.
- Frankcombe, L. M., and H. A. Dijkstra, 2009: Coherent multidecadal variability in North Atlantic sea level. *Geophys. Res. Lett.*, **36**, L15604, doi:10.1029/2009GL039455.
- Frankignoul, C., and K. Hasselmann, 1977: Stochastic climate models. Part II: Application to sea surface temperature anomalies and thermocline variability. *Tellus*, **29**, 289–305.
- , and P. Müller, 1979: Quasi-geostrophic response of an infinite beta-plane ocean to stochastic forcing by the atmosphere. *J. Phys. Oceanogr.*, **9**, 104–127.
- , —, and E. Zurita, 1997: A simple model of the decadal response of the ocean to stochastic wind forcing. *J. Phys. Oceanogr.*, **27**, 1533–1546.
- Griffies, S. M., and E. Tziperman, 1995: A linear thermohaline oscillator driven by stochastic atmospheric forcing. *J. Climate*, **8**, 2440–2453.
- Hawkins, E., and R. Sutton, 2009: Decadal predictability of the Atlantic Ocean in a coupled GCM: Forecast skill and optimal perturbations using linear inverse modeling. *J. Climate*, **22**, 3960–3978.
- Hirschi, J., and J. Marotzke, 2007: Reconstructing the meridional overturning circulation from boundary densities and the zonal wind stress. *J. Phys. Oceanogr.*, **37**, 743–763.
- Hurrell, J. W., and Coauthors, 2006: Atlantic climate variability and predictability: A CLIVAR perspective. *J. Climate*, **19**, 5100–5121.
- Jayne, S. R., and J. Marotzke, 2001: The dynamics of ocean heat transport variability. *Rev. Geophys.*, **3**, 384–411.
- Johns, W. E., and Coauthors, 2011: Continuous, array-based estimates of Atlantic Ocean heat transport at 26.5°N. *J. Climate*, **24**, 2429–2449.
- Jungclaus, J. H., H. Haak, M. Latif, and U. Mikolajewicz, 2005: Arctic–North Atlantic interactions and multidecadal variability of the meridional overturning circulation. *J. Climate*, **18**, 4013–4031.
- Kushnir, Y., 1994: Interdecadal variations in North Atlantic sea surface temperature and associated atmospheric condition. *J. Climate*, **7**, 141–157.
- Kwon, Y.-O., and C. Frankignoul, 2012: Stochastically-driven multidecadal variability of the Atlantic meridional overturning circulation in CCSM3. *Climate Dyn.*, **38**, 859–876.
- Mahajan, S., R. Zhang, and T. L. Delworth, 2011a: Impact of the Atlantic meridional overturning circulation (AMOC) on arctic surface air temperature and sea ice variability. *J. Climate*, **24**, 6573–6581.
- , —, —, S. Zhang, A. J. Rosati, and Y.-S. Chang, 2011b: Predicting Atlantic meridional overturning circulation (AMOC) variations using subsurface and surface fingerprints. *Deep-Sea Res.*, **58**, 1895–1903.
- Mann, C. R., 1967: The termination of the Gulf Stream and the beginning of the North Atlantic Current. *Deep-Sea Res.*, **14**, 337–359.
- Marshall, J., and F. Schott, 1999: Open-ocean convection: Observations, theory and models. *Rev. Geophys.*, **37**, 1–64.
- , and Coauthors, 2001a: North Atlantic climate variability: Phenomena, impacts, and mechanisms. *Int. J. Climatol.*, **21**, 1863–1898.
- , H. Johnson, and J. Goodman, 2001b: A study of the interaction of the North Atlantic Oscillation with ocean circulation. *J. Climate*, **14**, 1399–1421.
- Meinen, C. S., D. R. Watts, and R. A. Clarke, 2000: Absolutely referenced geostrophic velocity and transport on a section across the North Atlantic current. *Deep-Sea Res.*, **47**, 309–322.
- Msadek, R., K. W. Dixon, T. L. Delworth, and W. Hurlin, 2010: Assessing the predictability of the Atlantic meridional overturning circulation and associated fingerprints. *Geophys. Res. Lett.*, **37**, L19608, doi:10.1029/2010GL044517.
- Oka, A., and H. Hasumi, 2006: Effects of model resolution on salt transport through northern high-latitude passages and Atlantic meridional overturning circulation. *Ocean Modell.*, **13**, 126–147.
- Olsen, S. M., B. Hansen, D. Quadfasel, and S. Osterhus, 2008: Observed and modelled stability of overflow across the Greenland-Scotland ridge. *Nature*, **455**, 519–522.
- Sévellec, F., and A. V. Fedorov, 2011: Stability of the Atlantic meridional overturning circulation and stratification in a zonally-averaged ocean model: The effects of freshwater flux, wind stress, and diapycnal diffusion. *Deep-Sea Res.*, **58**, 1927–1943, doi:10.1016/j.dsr.2010.10.070.
- Te Raa, L. A., J. Gerrits, and H. A. Dijkstra, 2004: Identification of the mechanism of interdecadal variability in the North Atlantic Ocean. *J. Phys. Oceanogr.*, **34**, 2792–2807.
- Tulloch, R. T., J. C. Marshall, and K. S. Smith, 2009: Interpretation of the propagation of surface altimetric observations in terms of planetary waves and geostrophic turbulence. *J. Geophys. Res.*, **114**, C02005, doi:10.1029/2008JC005055.
- Tziperman, E., L. Zanna, and C. Penland, 2008: Non-normal thermohaline circulation dynamics in a coupled ocean–atmosphere GCM. *J. Phys. Oceanogr.*, **38**, 588–604.
- Weaver, A. J., and S. Valcke, 1998: On the variability of the thermohaline circulation in the GFDL coupled model. *J. Climate*, **11**, 759–767.
- , J. Marotzke, P. F. Cummins, and E. S. Sarachik, 1993: Stability and variability of the thermohaline circulation. *J. Phys. Oceanogr.*, **23**, 39–60.
- Yeager, S. G., and G. Danabasoglu, 2012: Sensitivity of Atlantic meridional overturning circulation variability to parameterized Nordic Sea overflows in CCSM4. *J. Climate*, **25**, 2077–2103.
- Yoshimori, M., C. C. Raible, T. F. Stocker, and M. Renold, 2010: Simulated decadal oscillations of the Atlantic meridional overturning circulation in a cold climate state. *Climate Dyn.*, **34**, 101–121, doi:10.1007/s00382-009-0540-9.
- Zhang, D., R. Msadek, M. J. McPhaden, and T. L. Delworth, 2011: Multidecadal variability of the North Brazil Current and its connection to the Atlantic meridional overturning circulation. *J. Geophys. Res.*, **116**, C04012, doi:10.1029/2010JC006812.
- Zhang, R., 2008: Coherent surface-subsurface fingerprint of the Atlantic meridional overturning circulation. *Geophys. Res. Lett.*, **35**, L20705, doi:10.1029/2008GL035463.
- Zhu, X., and J. Jungclaus, 2008: Interdecadal variability of the meridional overturning circulation as an ocean internal mode. *Climate Dyn.*, **31**, 731–741, doi:10.1007/s00382-008-0383-9.